

A Hybrid SIE-PDE Formulation Without Boundary Condition Requirement for Electromagnetic Analysis

Aipeng Sun^a, Zekun Zhu^a, Shunchuan Yang^{b,a,*}

^a*School of Electronic Information Engineering, Beihang University, Xueyuan Road 37, Haidian District, Beijing, China*

^b*Research Institute for Frontier Science, Beihang University, Xueyuan Road 37, Haidian District, Beijing, China*

Abstract

A hybrid surface integral equation partial differential equation (SIE-PDE) formulation without the boundary condition requirement is proposed to solve the electromagnetic problems. In the proposed formulation, the computational domain is decomposed into two *overlapping* domains: the SIE and PDE domains. In the SIE domain, complex structures with piecewise homogeneous media, e.g., highly conductive media, are included. An equivalent model for those structures is constructed through replacing them by the background medium and introducing a surface equivalent electric current density on an enclosed boundary to represent their electromagnetic effects. The remaining computational domain and homogeneous background medium replaced domain consist of the PDE domain, in which inhomogeneous or non-isotropic media are included. Through combining the surface equivalent electric current density and the inhomogeneous Helmholtz equation, a hybrid SIE-PDE formulation is derived. Unlike other hybrid formulations, where the transmission condition is usually used, no boundary conditions are required in the proposed SIE-PDE formulation, and it is mathematically equivalent to the original physical model. Through careful construction of basis functions to expand electric fields and the equivalent current density, the discretized formulation is compatible on the interface of the SIE and PDE domain. Finally, its accuracy and efficiency are validated through two numerical examples. Results show that the proposed SIE-PDE formulation can obtain accurate results including both near and far fields, and significant performance improvements in terms of CPU time and memory consumption compared with the FEM are achieved.

Keywords: finite element method, hybrid methods, method of moment, partial differential equation, surface equivalence theorem, surface integral equation

1. Introduction

Hybrid formulations show significant potential in solving challenging problems in electrical engineering fields, like scattering from multiscale and electrically large objects [1], parameters extraction in integrated circuits [2], since they can inherit the merits and overcome possible disadvantages of each formulation. They attract much attention in the last two decades, and a number of formulations are developed in the computational electromagnetics. Those formulations can be categorized into time-domain methods, like the hybrid finite-difference time-domain finite-element time-domain (FDTD-FETD) method [3][4], the hybrid spectral element time-domain finite-element time-domain (SETD/FETD) method [5], the unconditionally stable finite-element time-domain (US-FETD) method [6], and the finite-element time-domain generalized scattering matrix (FETD-GSM) method [7], and frequency-domain methods, like the method of moment mode-matching (MoM/MM) method [8][9], the method of moment physical-optics (MoM-PO) method [10-12], and the finite-element method/method of moment (FEM/MoM)[13-18], which can efficiently solve

*Corresponding author

Email address: scyang@buaa.edu.cn (Shunchuan Yang)

various electromagnetic problems. In this paper, we do not intend to review all of those hybrid formulations, but mainly focus on those in the frequency domain, especially, the hybrid FEM-MoM formulations.

One main group of hybrid formulations in the frequency domain is to combine different types of integral equations, like the MoM/PO method [10-12], the method of moment uniform geometrical theory of diffraction (MoM/UTD) method [19][20], to solve the scattering problems induced by the electrically large and multiscale objects, and extract the electrical parameters from integrated circuits, which are quite efficient to model structures with piecewise homogeneous media. However, they are incapable of handling objects with inhomogeneous or non-isotropic media since the surface equivalence theorem is not applicable. To mitigate this issue, another group of hybrid formulations is to combine the finite element and boundary integral formulations, like the FEM/MoM [13-18], the finite element boundary integral (FE-BI) formulation [21][22]. In those hybrid FE-BI formulations, the surface integral equation (SIE) formulation is often used to mimic the absorbing boundary conditions and truncate the computational domain in the FEM. Typical applications are the scalar FE-BI [23], and its symmetrical version [24][25], which are proposed to improve the efficiency, accuracy, and convergence properties. In [27][28], the SIE formulation is used to model the electrically large structures with homogeneous media, and the FEM is for geometrically fine structures or inhomogeneous media. In those formulations, the computational domain is decomposed into two *non-overlapping* domains: one for the BEM formulation and the other for the FEM formulation. A boundary condition, e.g., the second kind of boundary condition [29, Ch. 1, pp. 42-46], or the transmission condition [29, Ch. 14, pp. 1066-1083], is required to couple the FEM and BEM formulations on the interface of the two domains. Certain assumptions are required to ensure that electromagnetic fields meet those boundary conditions. However, such assumptions are not always satisfied in the practical physical fields. Therefore, they may suffer from the accuracy issue for near fields calculation, and are mainly used to calculate far fields [27][28].

In essence, those formulations can be cast into the domain decomposition methods (DDMs), which implies that different formulations can be applied in the corresponding domains according to their geometrical and material properties [30-33]. Especially, one embedded domain decomposition method (DDM) is proposed for signal integrity design and electromagnetic scattering analysis in [34][35]. The computational domain is decomposed into two *overlapping* domains: mesh coarse and fine domains. The geometrically fine structures are placed in the mesh fine domain and moved away from the computational domain. Therefore, the remaining computational domain does not include the geometrically fine structures, and coarse mesh can be used. The transmission condition is used to couple fields between the two domains. It shows significant performance improvements in terms of CPU time and memory consumption. However, it may need several iterations to solve the problems and suffer from efficiency issues if the boundary condition is not properly handled [34][35].

To mitigate the above accuracy and efficiency issues in the existing hybrid formulations, a novel hybrid SIE-PDE formulation without boundary condition requirement is proposed for electromagnetic analysis. The computational domain is first decomposed into two *overlapping* domains like the embedded DDM. One domain is for the SIE formulation, which is bounded by an enclosed contour, and the other domain is for the PDE formulation, which includes the whole computational domain. In the SIE domain, an equivalent model is derived based on the surface equivalent theorem [36, Ch. 12, pp. 653-658]. The original structures are replaced by the background medium, and the surface equivalent electric current density is introduced on the boundary to keep fields unchanged in the exterior region. In the PDE domain, the inhomogeneous Helmholtz formulation incorporated with the surface equivalent electric current density on the boundary of the SIE domain is used to model inhomogeneous or non-isotropic media. Therefore, the electromagnetic fields in the whole computational domain can be formulated through a hybrid SIE-PDE formulation. Complex structures and computationally challenging media, like the highly conductive media, are replaced by the background medium, which can be easily handled with coarse meshes. Therefore, the proposed SIE-PDE formulation can significantly improve the efficiency over the traditional PDE formulations. Compared with other hybrid FEM-MoM formulations or the FE-BI formulations, which require fictitious boundary conditions to couple the different formulations, the proposed SIE-PDE formulation is mathematically equivalent to the original physical model, and no additional boundary conditions are required. Therefore, accurate near and far fields can be obtained.

This paper is organized as follows. In Section 2, configurations and preliminary notations are defined,

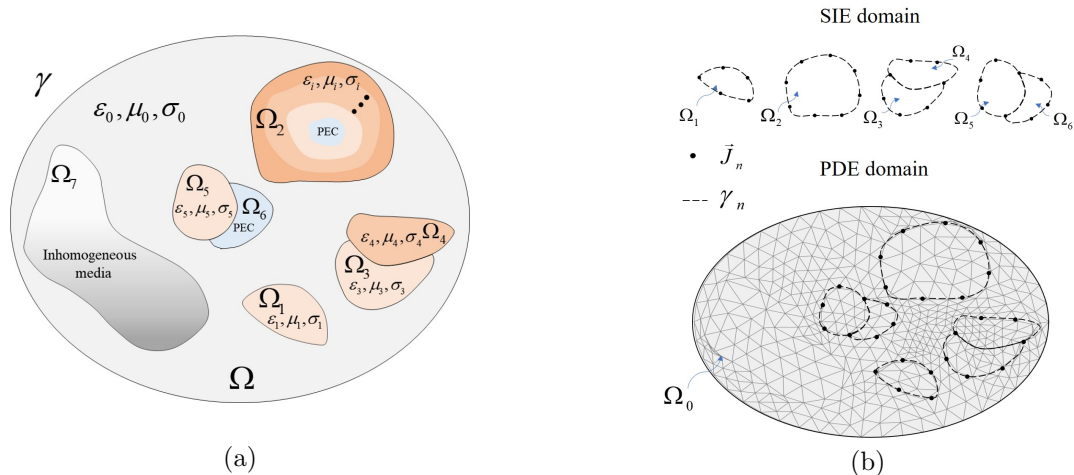


Figure 1: (a) The general scenario including complex structures with homogeneous and inhomogeneous media, and (b) the *overlapping* SIE and PDE domains for the proposed hybrid SIE-PDE formulation.

and procedures for the proposed hybrid SIE-PDE formulation are illustrated. In Section 3, the hybrid SIE-PDE formulation is proposed. In Section 4, detailed implementations for the proposed hybrid SIE-PDE formulation are shown. In addition, fields calculation in the whole computational domain is also discussed. In Section 5, two numerical examples are carried out to validate its accuracy and efficiency. At last, we draw some conclusions in Section 6.

2. Configurations and Preliminaries

In this paper, as shown in Fig. 1(a), a general scenario with the two-dimensional transverse magnetic (TM) scattering problem induced by objects with homogeneous and inhomogeneous media is considered to demonstrate the proposed SIE-PDE formulation. The constant parameters of those objects are the permittivity ε_i , the permeability μ_i and the conductivity σ_i , respectively, and its corresponding boundary is γ_i . The background medium is air with constant parameters of $\varepsilon_0, \mu_0, \sigma_0$, and the whole computational domain is truncated by the outermost boundary γ .

A character with a subscript, e.g. E_i , denotes a continuous quantity on γ_i . A hollow character with a subscript, e.g. \mathbb{P}_i , denotes a matrix on γ_i , and a bold character with a subscript, e.g. \mathbf{E}_i , denotes a column vector on γ_i . Quantities with $\hat{\cdot}$, e.g. \hat{E} , are used for the equivalent model.

The proposed hybrid SIE-PDE formulation needs the following three steps:

- 1) An appropriate boundary γ_n is selected, and the computational domain is decomposed into two *overlapping* domains: the SIE domain, which includes complex structures or computationally challenging media, and the PDE domain, in which inhomogeneous and non-isotropic media are filled as shown in Fig. 1.
- 2) In the SIE domain, an equivalent model is constructed through applying the surface equivalence theorem, and single surface electric current density J_n is derived and enforced on γ_n .
- 3) In the PDE domain, which includes the remaining computational domain and the background medium replaced domain, the inhomogeneous Helmholtz equation in terms of electric fields is used to model inhomogeneous and non-isotropic media. In addition, the surface equivalent electric current density on γ_n is coupled into the Helmholtz equation to present the electromagnetic effects in the SIE domain. Then, the hybrid SIE-PDE formulation without the boundary condition requirement is derived.

In the following section, we first derive the equivalent model incorporated with the single electric current density, and then derive the hybrid SIE-PDE formulation in terms of electric fields in the continuous physical domain.

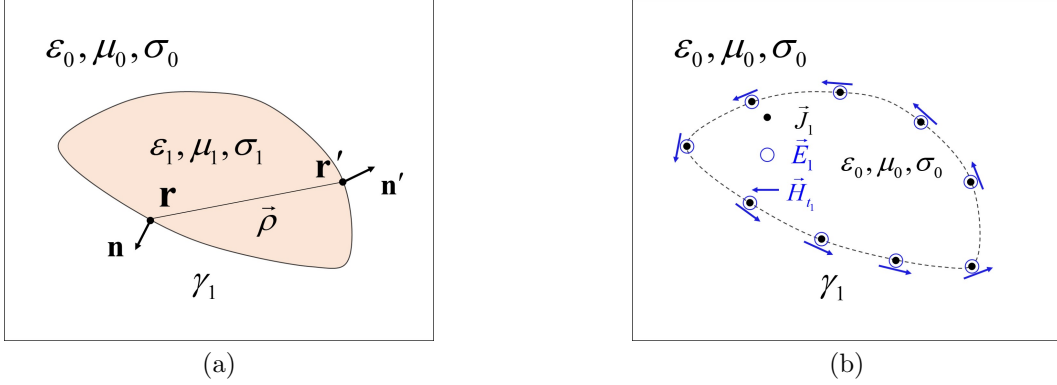


Figure 2: (a) The original model for a single penetrable object, and (b) the equivalent model.

3. The Proposed Hybrid SIE-PDE Formulation

3.1. The Equivalent Model with the Single Electric Current Density for Objects with Piecewise Homogeneous Media in the SIE Domain

We first illustrate the detailed derivation of the equivalent model with the single electric current density for objects with piecewise homogeneous media. To make the derivation concise, a single penetrable object with the permittivity ε_1 , the permeability μ_1 , and the conductivity σ_1 is first considered, as shown in Fig. 2(a). Its boundary is denoted as γ_1 . According to the surface equivalence theorem [36, Ch. 12, pp. 653-658], an equivalent model can be obtained, in which the object is replaced by its surrounding medium, and a surface equivalent electric current density is introduced on γ_1 . To further enforce the electric fields in the original and equivalent configurations equal to each other on γ_1 , a single-source (SS) formulation with only the electric current density on γ_1 is obtained in Fig. 2(b) [37].

Without loss of generality, the penetrable object does not include any sources. Therefore, the electric fields inside the penetrable object must satisfy the following homogeneous scalar Helmholtz equation

$$\nabla^2 E_1 + k^2 E_1 = 0, \quad (1)$$

subject to the boundary condition

$$E_1(\mathbf{r})|_{\mathbf{r} \in \gamma_1} = \widehat{E}_1(\mathbf{r})|_{\mathbf{r} \in \gamma_1}, \quad (2)$$

where E_1 , \widehat{E}_1 denote the electric fields inside γ_1 for the original and equivalent models, respectively, and $E_1(\mathbf{r})|_{\mathbf{r} \in \gamma_1}$, $\widehat{E}_1(\mathbf{r})|_{\mathbf{r} \in \gamma_1}$ denote their values on the inner side of γ_1 .

(1) can be solved through the contour integral method [38]. Then, the electric fields inside γ_1 can be expressed in terms of E_1 and its normal derivative on γ_1 as

$$TE_1(\mathbf{r}) = \oint_{\gamma_1} \left[G_1(\mathbf{r}, \mathbf{r}') \frac{\partial E_1(\mathbf{r}')}{\partial n'} - E_1(\mathbf{r}') \frac{\partial G_1(\mathbf{r}, \mathbf{r}')}{\partial n'} \right] d\mathbf{r}', \quad (3)$$

where $T = 1/2$, when the source point \mathbf{r}' and the observation point \mathbf{r} are located on the same boundary, otherwise, $T = 1$. $G_1(\mathbf{r}, \mathbf{r}')$ is the Green's function, which is given by $G_1(\mathbf{r}, \mathbf{r}') = -jH_0^{(2)}(k_1\rho)/4$, where $j = \sqrt{-1}$, $\rho = |\mathbf{r} - \mathbf{r}'|$, k_1 denotes the wave number in the penetrable object, and $H_0^{(2)}(\cdot)$ denotes the zeroth-order Hankel function of the second kind. \mathbf{n} , \mathbf{n}' denote the unit normal vector pointing outward γ_1 at the observation point \mathbf{r} and the source point \mathbf{r}' , respectively. In addition, the tangential magnetic field on γ_1 , which is related to the electric field through the Poincare-Steklov operator [39], can be written as

$$H_{t_1}(\mathbf{r}) = \frac{1}{j\omega\mu_1} \frac{\partial E_1(\mathbf{r})}{\partial n} \Big|_{\mathbf{r} \in \gamma_1}, \quad (4)$$

where μ_1 is the permeability of the penetrable object. We introduce the surface admittance operator (SAO) \mathcal{Y} [40], which relates the normal derivative of electric fields to electric fields on γ_1 . Therefore, it can be expressed as

$$\left. \frac{\partial E_1(\mathbf{r})}{\partial n} \right|_{\mathbf{r} \in \gamma_1} = \mathcal{Y}_1 E_1|_{\mathbf{r} \in \gamma_1}. \quad (5)$$

By substituting (5) into (3), we have

$$T E_1(\mathbf{r}) = \oint_{\gamma_1} \left[G_1(\mathbf{r}, \mathbf{r}') \mathcal{Y}_1 - \frac{\partial G_1(\mathbf{r}, \mathbf{r}')}{\partial n'} \right] E_1(\mathbf{r}') d\mathbf{r}'. \quad (6)$$

To make the derivation more concise, we borrow some notations from [40]. Then, (6) is compactly expressed in an operator format as

$$T E_1 = (g_1 \mathcal{Y}_1 - g_{1n'}) E_1, \quad (7)$$

where g_1 , $g_{1n'}$ denote the integral operators for the Green's function and its normal derivative on γ_1 , respectively. Their expressions are given by

$$\begin{aligned} g_1 &= \oint_{\gamma_1} G_1(\mathbf{r}, \mathbf{r}') (\cdot) d\mathbf{r}', \\ g_{1n'} &= \oint_{\gamma_1} \left[\frac{\partial G_1(\mathbf{r}, \mathbf{r}')}{\partial n'} \right] (\cdot) d\mathbf{r}'. \end{aligned} \quad (8)$$

After moving the second term of (7) on its right hand side (RHS) to its left hand side (LHS) and inverting the integral operator g_1 , \mathcal{Y}_1 can be expressed as

$$\mathcal{Y}_1 = g_1^{-1} (T I + g_{1n'}), \quad (9)$$

where I is the identity operator. Therefore, (4) can be rewritten via the SAO as

$$H_{t_1}(\mathbf{r}) = \frac{1}{j\omega\mu_1} \mathcal{Y}_1 E_1|_{\mathbf{r} \in \gamma_1}. \quad (10)$$

Then, the surface equivalence theorem is applied through replacing the penetrable object inside γ_1 by its surrounding medium. The equivalent model with only the single electric current density is derived, as shown in Fig. 2(b), and $\hat{\mathcal{Y}}_1$ can be expressed as

$$\hat{\mathcal{Y}}_1 = \hat{g}_1^{-1} (T I + \hat{g}_{1n'}). \quad (11)$$

The tangential magnetic field $\hat{H}_{t_1}(\mathbf{r})$ on γ_1 can also be achieved through the SAO in the equivalent model

$$\hat{H}_{t_1}(\mathbf{r}) = \frac{1}{j\omega\mu_0} \hat{\mathcal{Y}}_1 \hat{E}_1|_{\mathbf{r} \in \gamma_1}. \quad (12)$$

Since the boundary condition (2) is enforced, the magnetic current density in the equivalent configuration vanishes, and only the electric current density J_1 is introduced on γ_1 to keep fields outside γ_1 unchanged. According to the surface equivalence theorem [36, Ch. 12, pp. 653-658], the equivalent electric current density J_1 is expressed as

$$J_1 = H_{t_1}(\mathbf{r}) - \hat{H}_{t_1}(\mathbf{r}). \quad (13)$$

By substituting (10) and (12) into (13), J_1 can be rewritten as

$$J_1 = \underbrace{\left(\frac{1}{j\omega\mu_1} \mathcal{Y}_1 - \frac{1}{j\omega\mu_0} \hat{\mathcal{Y}}_1 \right)}_{\mathcal{Y}_{s_1}} E_1|_{\mathbf{r} \in \gamma_1}, \quad (14)$$

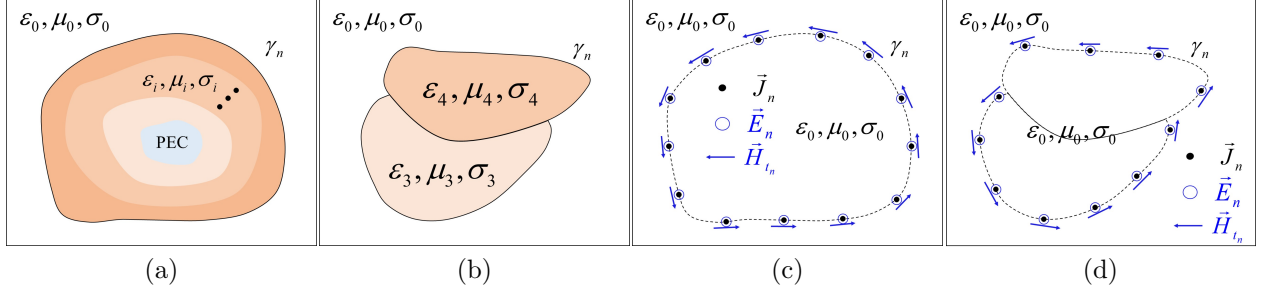


Figure 3: (a) The original object embedded into multilayer dielectric media, (b) the original partial connected penetrable objects, (c) the equivalent model for object embedded into multilayer dielectric media, and (d) the equivalent model for partial connected penetrable objects.

where \mathcal{Y}_{s_1} is the differential surface admittance operator (DSAO) [41] defined on γ_1 . (14) relates the surface equivalent electric current density J_1 to electric fields E_1 on γ_1 .

When complex objects embedded in multilayers, composite structures with partial connected penetrable and PEC objects are involved in the SIE domain, as shown in Fig. 3(a) and (b), equivalent models with only the electric current density J_n can still be derived through replacing those objects by the background medium, as shown in Fig. 3(c) and (d). Interested readers are referred to [37][42] for more details to obtain the equivalent models.

In a word, the tangential magnetic fields on γ_n for the original and equivalent models can also be achieved through the SAO given by

$$H_{t_n}(\mathbf{r}) = \frac{1}{j\omega\mu_n} \mathcal{Y}_n E_n|_{\mathbf{r} \in \gamma_n}, \quad (15)$$

$$\hat{H}_{t_n}(\mathbf{r}) = \frac{1}{j\omega\mu_0} \hat{\mathcal{Y}}_n \hat{E}_n|_{\mathbf{r} \in \gamma_n}. \quad (16)$$

where H_{t_n} , \hat{H}_{t_n} , E_n , \hat{E}_n , \mathcal{Y}_n , $\hat{\mathcal{Y}}_n$ denote the tangential magnetic fields and electric fields on γ_n , and the SAO for the original and equivalent models, respectively.

Similar to the boundary condition (2), we also enforce $E_n(\mathbf{r})|_{\mathbf{r} \in \gamma_n} = \hat{E}_n(\mathbf{r})|_{\mathbf{r} \in \gamma_n}$ on γ_n . Then, the equivalent electric current density on γ_n can be derived and expressed as

$$J_n = \underbrace{\left(\frac{1}{j\omega\mu_n} \mathcal{Y}_n - \frac{1}{j\omega\mu_0} \hat{\mathcal{Y}}_n \right)}_{\mathcal{Y}_{s_n}} E_n|_{\mathbf{r} \in \gamma_n}, \quad (17)$$

where \mathcal{Y}_{s_n} is the DSAO defined on γ_n .

3.2. The PDE Formulation in the PDE Domain

In the PDE domain, inhomogeneous or non-isotropic media are possibly included. The electric fields E_0 satisfy the scalar inhomogeneous Helmholtz equation

$$\nabla^2 E_0 + k^2 E_0 = j\omega\mu J, \quad (18)$$

where J denotes the electric current density inside the computational domain, and μ , k denote the permeability and the wave number of the media inside the PDE domain, which may be a function of positions.

(18) can be expanded into its component form in TM mode as

$$\frac{\partial}{\partial x} \left(\frac{1}{\mu_r} \frac{\partial E_0}{\partial x} \right) + \frac{\partial}{\partial y} \left(\frac{1}{\mu_r} \frac{\partial E_0}{\partial y} \right) + k_0^2 \epsilon_r E_0 = j\omega\mu_0 J, \quad (19)$$

where k_0 is the wave number of the free space, and ϵ_r , μ_r are the relative permittivity and permeability of the media inside the PDE domain, respectively.

3.3. The Hybrid SIE-PDE Formulation for the Whole Computational Domain

The hybrid SIE-PDE formulation can be derived through the following procedures.

- 1) In the SIE domain, the surface equivalence theorem is used to derive an equivalent model with only the electric current density J_n on γ_n by incorporating the DSAO. It is general and applicable for the single penetrable objects, objects embedded in multilayers, and arbitrarily connected penetrable and PEC objects [37][42].
- 2) After that, the electric current density J_n is used as an excitation in the inhomogeneous Helmholtz equation to couple the SIE and PDE formulations. Therefore, (19) is modified as

$$\frac{\partial}{\partial x} \left(\frac{1}{\mu_r} \frac{\partial E_0}{\partial x} \right) + \frac{\partial}{\partial y} \left(\frac{1}{\mu_r} \frac{\partial E_0}{\partial y} \right) + k_0^2 \varepsilon_r E_0 - j\omega\mu_0 J_n = j\omega\mu J, \quad (20)$$

where μ_0 is the permeability of the background medium. By substituting (17) into (20), it can be further rewritten as

$$\frac{\partial}{\partial x} \left(\frac{1}{\mu_r} \frac{\partial E_0}{\partial x} \right) + \frac{\partial}{\partial y} \left(\frac{1}{\mu_r} \frac{\partial E_0}{\partial y} \right) + k_0^2 \varepsilon_r E_0 - j\omega\mu_0 \mathcal{Y}_{s_n} E_n|_{\mathbf{r} \in \gamma_n} = j\omega\mu J. \quad (21)$$

Therefore, the governing equation for the whole computational domain is finally derived. It can be found that the SIE and PDE formulations are coupled through the surface equivalent electric current density, which does not require additional boundary conditions, e.g., the transmission condition, as other techniques, like the FEM-MoM method [13-18], the FE-BI formulation [21-25], and the multi-region multi-solver [27][28]. The proposed hybrid SIE-PDE formulation is mathematically equivalent to the original physical model. Therefore, through solving (21), all the electric fields of the computational domain can be accurately calculated. It should be noted that although E_0 exist in the whole computational domain, they are invalid in the homogeneous background medium replaced domain, in which fictitious fields are obtained, since the surface equivalence theorem is used. In the later section, we will discuss how to recover the electric fields inside the SIE domain.

4. Detailed Implementations of the Proposed Hybrid SIE-PDE Formulation

4.1. Construction of the Basis Functions for Electric Field Expansion

Before we discretize (21), the basis functions should be carefully selected to expand the electric fields. As is illustrated in Section 3.3, the computational domain is decomposed into two *overlapping* domains, and γ_n is the boundary of the SIE domain, where J_n resides in Fig. 3(c) and (d). In (17), we can find that \mathcal{Y}_{s_n} is used to relate the surface equivalent current density J_n to the tangential electric fields E_n on γ_n . In our implementation, the Galerkin scheme is used to solve (21). The challenging part is that the discretized hybrid SIE-PDE formulation should be compatible on the boundary γ_n , so that the electromagnetic effects of J_n can be directly imposed on the discretized Helmholtz equation. Since the linear basis functions are used to expand the electric fields in the PDE domain, the rooftop basis functions, which are constructed through combining the degenerated linear basis functions on γ_n from two adjacent triangle elements, are used to expand the equivalent current density J_n in Fig. 3(c) and (d).

The linear basis function in the two-dimensional space is defined on the triangular elements [29, Ch. 4, pp. 162-163] as

$$N_i^e(x, y) = \frac{1}{2\Delta^e} (a_j^e + b_j^e x + c_j^e y), \quad i = 1, 2, 3, \quad (22)$$

where

$$\begin{aligned} a_1^e &= x_2^e y_3^e - y_2^e x_3^e & b_1^e &= y_2^e - y_3^e & c_1^e &= x_3^e - x_2^e, \\ a_2^e &= x_3^e y_1^e - y_3^e x_1^e & b_2^e &= y_3^e - y_1^e & c_2^e &= x_1^e - x_3^e, \\ a_3^e &= x_1^e y_2^e - y_1^e x_2^e & b_3^e &= y_1^e - y_2^e & c_3^e &= x_2^e - x_1^e, \end{aligned}$$

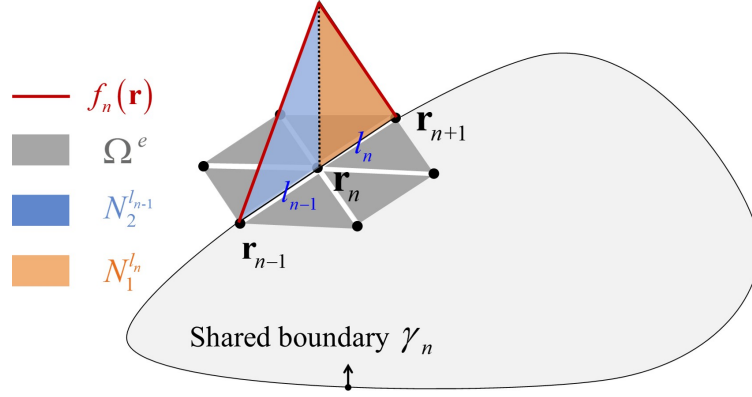


Figure 4: A general configuration to demonstrate the relationship between the linear basis function and the rooftop basis function on the share boundary γ_n . \mathbf{r}_{n-1} , \mathbf{r}_n , \mathbf{r}_{n+1} are the endpoints of the n th and $(n+1)$ th segments, $l_{n-1} = |\mathbf{r}_n - \mathbf{r}_{n-1}|$, $l_n = |\mathbf{r}_{n+1} - \mathbf{r}_n|$.

and

$$\Delta^e = \frac{1}{2} \begin{vmatrix} 1 & x_1^e & y_1^e \\ 1 & x_2^e & y_2^e \\ 1 & x_3^e & y_3^e \end{vmatrix} = \frac{1}{2} (b_1^e c_2^e - b_2^e c_1^e),$$

where x_i^e and y_i^e ($i = 1, 2, 3$) denote the coordinates in the x , y direction of the i th node of the e th triangle element, respectively, and Δ^e denotes the area of the e th element. It should be noted that N_i^e is locally supported, and only defined on the e th triangle element. On the boundary segment, the linear basis functions are degenerated into the following shape functions

$$N_1^{l_n} = \frac{|\mathbf{r}_{n+1} - \mathbf{r}|}{l_n}, \quad N_2^{l_n} = \frac{|\mathbf{r} - \mathbf{r}_n|}{l_n}, \quad \mathbf{r} \in [\mathbf{r}_n, \mathbf{r}_{n+1}]. \quad (23)$$

To make the discretized SIE formulation and the PDE formulation compatible on γ_n , the rooftop basis function through combining two adjacent triangle elements is defined at the node rather than on the segment, which can be expressed at the n th node as

$$f_n(\mathbf{r}) = \begin{cases} \frac{|\mathbf{r} - \mathbf{r}_{n-1}|}{l_{n-1}}, & \mathbf{r} \in [\mathbf{r}_{n-1}, \mathbf{r}_n] \\ \frac{|\mathbf{r}_{n+1} - \mathbf{r}|}{l_n}, & \mathbf{r} \in [\mathbf{r}_n, \mathbf{r}_{n+1}] \end{cases}. \quad (24)$$

Therefore, as shown in Fig. 4, the relationship between the linear basis function and the rooftop basis function can be expressed as

$$f_n(\mathbf{r}) = \begin{cases} N_2^{l_{n-1}}, & \mathbf{r} \in [\mathbf{r}_{n-1}, \mathbf{r}_n] \\ N_1^{l_n}, & \mathbf{r} \in [\mathbf{r}_n, \mathbf{r}_{n+1}] \end{cases}. \quad (25)$$

4.2. Discretization for the Proposed Hybrid SIE-PDE Formulation

To clearly explain the procedure of discretization for the proposed hybrid SIE-PDE formulation, let us consider the general scenario with a single penetrable object in Fig. 2(a). The penetrable object with the boundary γ_1 is located in the SIE domain, and its equivalent model is illustrated in detail in Section 3.1.

We first discretize γ_1 into m_1 segments and use the rooftop basis function to expand E_1 and H_{t_1} in (3) and (4) as

$$E_1(\mathbf{r}) = \sum_{n=1}^{m_1} e_{1n} f_n(\mathbf{r}), \quad (26)$$

$$H_{t_1}(\mathbf{r}) = \sum_{n=1}^{m_1} h_{1n} f_n(\mathbf{r}), \quad (27)$$

where $f_n(\mathbf{r})$ denotes the n th basis function defined in (24). After substituting (26) and (27) into (3) and testing (3) through the Galerkin scheme at each segment node, we collect all E_1 and H_{t_1} expansion coefficients into two column vectors \mathbf{E}_1 and \mathbf{H}_1 as

$$\mathbf{E}_1 = [e_{11} \quad e_{12} \quad \dots \quad e_{1m_1}]^T, \quad (28)$$

$$\mathbf{H}_1 = [h_{11} \quad h_{12} \quad \dots \quad h_{1m_1}]^T. \quad (29)$$

Then, (3) can be rewritten into the matrix form as

$$T\mathbb{L}_1 \mathbf{E}_1 = \mathbb{P}_1 \mathbf{H}_1 + \mathbb{U}_1 \mathbf{E}_1, \quad (30)$$

where the subscript 1 denotes that the testing procedure is applied on γ_1 , and the entities of \mathbb{L}_1 , \mathbb{P}_1 and \mathbb{U}_1 are expressed as

$$[\mathbb{L}_1]_{m,n} = \int_{\gamma_1^{m-1} + \gamma_1^m} f_m(\mathbf{r}) \int_{\gamma_1^{n-1} + \gamma_1^n} f_n(\mathbf{r}') dr' dr, \quad (31)$$

$$[\mathbb{P}_1]_{m,n} = j\omega\mu_1 \int_{\gamma_1^{m-1} + \gamma_1^m} f_m(\mathbf{r}) \int_{\gamma_1^{n-1} + \gamma_1^n} G_1(\mathbf{r}, \mathbf{r}') f_n(\mathbf{r}') dr' dr, \quad (32)$$

$$[\mathbb{U}_1]_{m,n} = \int_{\gamma_1^{m-1} + \gamma_1^m} f_m(\mathbf{r}) \int_{\gamma_1^{n-1} + \gamma_1^n} k_1 \frac{\vec{\rho} \cdot \hat{n}'}{\rho} G_1'(\mathbf{r}, \mathbf{r}') f_n(\mathbf{r}') dr' dr, \quad (33)$$

where $G_1' = -jH_1^{(2)}(k_1\rho)/4$.

In this paper, a modified singularity handling approach through combining the numerical Gaussian quadrature and analytical integration approaches is used to accurately and efficiently handle the singular and nearly singular integrals in (32) and (33). In this approach, the Hankel function and its gradient are evaluated by the small variable approximation when a predefined threshold is satisfied. Then, the analytical approach is used to compute the singular and nearly singular integration, and the Gaussian quadrature is applied in other non-singular integration. To make our paper more focused, the detailed techniques are listed in the appendix.

Then, through moving the second term of (30) on the RHS to its LHS and inverting the square coefficient matrix \mathbb{P}_1 , we obtain the SAO \mathbb{Y}_1 [41] as

$$\mathbf{H}_1 = \underbrace{[\mathbb{P}_1]^{-1} (T\mathbb{L}_1 - \mathbb{U}_1)}_{\mathbb{Y}_1} \mathbf{E}_1. \quad (34)$$

In the equivalent configurations in Fig. 2(b), $\widehat{H}_{t_1}(\mathbf{r})$ can be also expanded through the rooftop basis function as

$$\widehat{H}_{t_1}(\mathbf{r}) = \sum_{n=1}^{m_1} \widehat{h}_{1n} f_n(\mathbf{r}). \quad (35)$$

With the similar procedures in the original object, we have

$$\widehat{\mathbf{H}}_1 = \underbrace{[\widehat{\mathbb{P}}_1]^{-1} (T\widehat{\mathbb{L}}_1 - \widehat{\mathbb{U}}_1)}_{\widehat{\mathbb{Y}}_1} \mathbf{E}_1, \quad (36)$$

where

$$\widehat{\mathbf{H}}_1 = \begin{bmatrix} \widehat{h}_{11} & \widehat{h}_{12} & \dots & \widehat{h}_{1m_1} \end{bmatrix}^T. \quad (37)$$

Since (2) is enforced on γ_1 , only the surface equivalent electric current density J_1 is required on γ_1 in the equivalent configuration to keep fields outside γ_1 unchanged. It can also be expanded through the rooftop basis function, and the coefficients are collected into the column vector \mathbf{J}_1 as

$$\mathbf{J}_1 = \begin{bmatrix} j_{11} & j_{12} & \dots & j_{1m_1} \end{bmatrix}^T. \quad (38)$$

By substituting (34) and (36) into (13), \mathbf{J}_1 is obtained as

$$\mathbf{J}_1 = \mathbb{Y}_{s_1} \mathbf{E}_1, \quad (39)$$

where \mathbb{Y}_{s_1} is the DSAO [41], and can be expressed as

$$\mathbb{Y}_{s_1} = \mathbb{Y}_1 - \widehat{\mathbb{Y}}_1 = [\mathbb{P}_1]^{-1} (T\mathbb{L}_1 - \mathbb{U}_1) - \left[\widehat{\mathbb{P}}_1 \right]^{-1} (T\mathbb{L}_1 - \widehat{\mathbb{U}}_1). \quad (40)$$

As shown in Fig. 3(a) and (b), when complex objects embedded in multilayers or composite objects with partial connected penetrable objects and PEC objects are involved in the SIE domain, \mathbf{J}_n on γ_n can also be derived according to the surface equivalence theorem [36, Ch. 12, pp. 653-658] in Fig. 3(c) and (d), which can be expressed as

$$\mathbf{J}_n = \mathbb{Y}_{s_n} \mathbf{E}_n. \quad (41)$$

Detailed formulations of \mathbb{Y}_{s_n} on γ_n can be found in [37][42]. Interested readers are referred to them for more details.

The remaining computational domain and homogenous background medium replaced domain are treated as the PDE domain, and the scalar inhomogeneous Helmholtz equation in terms of the electric fields E_0 is expressed in (20). We apply the Galerkin scheme to deriving the discretized formulation. By moving the excitation term of (20) on the RHS to its LHS, the residual error is defined as

$$r = \frac{\partial}{\partial x} \left(\frac{1}{\mu_r} \frac{\partial E_0}{\partial x} \right) + \frac{\partial}{\partial y} \left(\frac{1}{\mu_r} \frac{\partial E_0}{\partial y} \right) + k_0^2 \varepsilon_r E_0 - j\omega\mu_0 J_n - j\omega\mu J, \quad (42)$$

The PDE domain is discretized into M triangle elements, and the triangle meshes are compatible with segments on γ_n , as shown in Fig. 4. In each triangle element, E_0 can be approximated as

$$E_0^e(x, y) = \sum_{j=1}^3 N_j^e(x, y) E_{0j}^e, \quad e = 1, 2, \dots, M. \quad (43)$$

The weighted residual on the i th triangle element can be expressed as

$$R_i^e = \iint_{\Omega^e} N_i^e r dx dy, \quad i = 1, 2, 3, \quad (44)$$

where Ω^e is the i th element, and N_i^e are the two-dimensional linear basis functions given by (22). By substituting (42) into (44) and applying the divergence theorem [29, Ch. 4, pp. 154-157], (44) can be rewritten as

$$\begin{aligned} R_i^e = & \iint_{\Omega^e} \left(-\frac{1}{\mu_r^e} \frac{\partial N_i^e}{\partial x} \frac{\partial E_0}{\partial x} - \frac{1}{\mu_r^e} \frac{\partial N_i^e}{\partial y} \frac{\partial E_0}{\partial y} + k_0^2 \varepsilon_r^e N_i^e E_0 \right) dx dy \\ & - j\omega\mu_0 \iint_{\Omega^e} N_i^e J_n dx dy - j\omega\mu \iint_{\Omega^e} N_i^e J dx dy + \oint_{\Gamma^e} N_i^e \mathbf{D} \cdot \mathbf{n}^e d\Gamma, \end{aligned} \quad (45)$$

where ε_r^e , μ_r^e denote the relative permittivity and permeability of the e th triangle element, Γ^e denotes the contour of Ω^e , \mathbf{n}^e is the unit normal vector pointing outward Γ^e , and

$$\mathbf{D} = \left(\frac{1}{\mu_r} \frac{\partial E_0}{\partial x} \mathbf{x} + \frac{1}{\mu_r} \frac{\partial E_0}{\partial y} \mathbf{y} \right). \quad (46)$$

By substituting (43) into (45), the elemental equation is expressed as

$$\begin{aligned} R_i^e = & \sum_{j=1}^3 \iint_{\Omega^e} \left(-\frac{1}{\mu_r^e} \frac{\partial N_i^e}{\partial x} \frac{\partial N_j^e}{\partial x} - \frac{1}{\mu_r^e} \frac{\partial N_i^e}{\partial y} \frac{\partial N_j^e}{\partial y} + k_0^2 \varepsilon_r^e N_i^e N_j^e \right) E_{0j}^e dx dy \\ & - j\omega\mu_0 \iint_{\Omega^e} N_i^e J_n dx dy - j\omega\mu \iint_{\Omega^e} N_i^e J dx dy + \oint_{\Gamma^e} N_i^e \mathbf{D} \cdot \mathbf{n}^e d\Gamma, \end{aligned} \quad (47)$$

As is illustrated in Section 3, J_n only exists on γ_n . Therefore, it can also be approximated with the linear basis function on γ_n as

$$J_n^s(x, y) = \sum_{j=1}^2 N_j^{l_s}(x, y) J_{n_j}^s, \quad s = 1, 2, \dots, m_n. \quad (48)$$

Therefore, the integration terms of J_n is reduced into one-dimensional space, and (45) can be rewritten as

$$\begin{aligned} R_i^e = & \sum_{j=1}^3 \iint_{\Omega^e} \left(-\frac{1}{\mu_r^e} \frac{\partial N_i^e}{\partial x} \frac{\partial N_j^e}{\partial x} - \frac{1}{\mu_r^e} \frac{\partial N_i^e}{\partial y} \frac{\partial N_j^e}{\partial y} + k_0^2 \varepsilon_r^e N_i^e N_j^e \right) E_{0j}^e dx dy \\ & - j\omega\mu_0 \sum_{j=1}^2 \left(\int_{\gamma_n^s} N_i^{l_s} N_j^{l_s} \right) J_{n_j}^s dx dy - j\omega\mu \iint_{\Omega^e} N_i^e J dx dy + \oint_{\Gamma^e} N_i^e \mathbf{D} \cdot \mathbf{n}^e d\Gamma, \end{aligned} \quad (49)$$

which can be written in the matrix form as

$$\mathbf{R}^e = -\mathbb{K}^e \mathbf{E}^e - \mathbb{B}^s \mathbf{J}_n^s - \mathbf{b}^e + \mathbf{g}^e, \quad (50)$$

where

$$\mathbf{R}^e = [R_1^e \quad R_2^e \quad R_3^e]^T, \quad \mathbf{E}^e = [E_{01}^e \quad E_{02}^e \quad E_{03}^e]^T, \quad \mathbf{J}_n^s = [J_{n1}^s \quad J_{n2}^s]^T.$$

The entities of \mathbb{K}^e , \mathbb{B}^s , \mathbf{b}^e and \mathbf{g}^e are given by

$$[\mathbb{K}^e]_{i,j} = \iint_{\Omega^e} \left(-\frac{1}{\mu_r^e} \frac{\partial N_i^e}{\partial x} \frac{\partial N_j^e}{\partial x} - \frac{1}{\mu_r^e} \frac{\partial N_i^e}{\partial y} \frac{\partial N_j^e}{\partial y} + k_0^2 \varepsilon_r^e N_i^e N_j^e \right) dx dy, \quad i, j = 1, 2, 3, \quad (51)$$

$$[\mathbb{B}^s]_{i,j} = j\omega\mu_0 \int_{\gamma_n^s} N_i^{l_s} N_j^{l_s} dx dy, \quad i, j = 1, 2, \quad (52)$$

$$[\mathbf{b}^e]_i = j\omega\mu \iint_{\Omega^e} N_i^e J dx dy, \quad i = 1, 2, 3, \quad (53)$$

$$[\mathbf{g}^e]_i = \oint_{\Gamma^e} N_i^e \mathbf{D} \cdot \mathbf{n}^e d\Gamma, \quad i = 1, 2, 3. \quad (54)$$

Then, the final matrix equation can be obtained by assembling (50) for all elements, given by

$$\mathbf{R} = -\mathbb{K}\mathbf{E} - \mathbb{B}\mathbf{J}_n - \mathbf{b} + \mathbf{g}. \quad (55)$$

By enforcing that the residual error vanishes on all the elements, (55) can be written as

$$\mathbb{K}\mathbf{E} + \mathbb{B}\mathbf{J}_n = \mathbf{g} - \mathbf{b}. \quad (56)$$

By substituting (41) into (56), it can be rewritten as

$$\mathbb{K}\mathbf{E} + \mathbb{B}\mathbb{Y}_{s_n}\mathbf{E}_n = \mathbf{g} - \mathbf{b}. \quad (57)$$

It should be noted that $E_n(\mathbf{r})|_{\mathbf{r} \in \gamma_n} = E_0(\mathbf{r})|_{\mathbf{r} \in \gamma_n}$. Therefore, the second term of (57) on the LHS can be expanded through replacing \mathbf{E}_n by \mathbf{E} , and the discretized SIE-PDE formulation can be obtained as

$$(\mathbb{K} + \mathbb{A})\mathbf{E} = \mathbf{g} - \mathbf{b}, \quad (58)$$

where \mathbb{A} denotes the expansion matrix for $\mathbb{B}\mathbb{Y}_{s_n}$. Through solving (58), we can obtain the electric fields in the PDE domain. Other interested parameters, like near fields, the radar cross section (RCS) can be calculated. In the following subsection, we briefly discuss how to calculate the electric fields in the whole computational domain.

4.3. Fields Calculation in the Whole Computational Domain

By solving (58), the electric fields in the PDE domain are obtained. However, since the surface equivalence theorem is applied, the electric fields inside the SIE domain cannot be derived directly from the proposed SIE-PDE formulation. Therefore, electric fields inside the SIE domain should be carefully recovered. As illustrated in Section 4.2, if the objects are embedded in multilayers, or composite objects with partially connected penetrable objects and PEC objects are involved, electric fields inside the SIE domain can be calculated through the reverse procedure used to construct the equivalent model. More details can be found in [37][42].

5. Numerical Results and Discussion

All numerical examples in this paper are performed on a workstation with an Intel i7-7700 3.6 GHz CPU and 64 G memory. Our in-house codes are written in the Matlab. To make a fair comparison, only a single thread without any parallel computation is used to complete the simulations.

5.1. Accuracy Verification of the Proposed Hybrid SIE-PDE Formulation for Penetrable Structures

To verify the accuracy of the proposed SIE-PDE formulation, we first consider TM scattering problems induced by simple penetrable objects. The homogeneous background medium is chosen to simplify the verification. Two dielectric objects, an infinite long dielectric cylinder and cuboid with the relative permittivity $\varepsilon_r = 2.3$, are selected. Both objects are located in the air. The first-order absorbing boundary condition [29, Ch. 4, pp. 207-212] is used to truncate the computational domain in the FEM and the proposed SIE-PDE formulation, which is expressed as

$$\frac{1}{\mu_r} \frac{\partial E_0}{\partial n} + \gamma E_0 = q, \quad (59)$$

with γ and q given by

$$\gamma = \frac{1}{\mu_r} \left[jk_0 + \frac{\kappa(s)}{2} \right],$$

$$q = \frac{1}{\mu_r} \frac{\partial E^{inc}}{\partial n} + \frac{1}{\mu_r} \left[jk_0 + \frac{\kappa(s)}{2} \right] E^{inc},$$

where $\kappa(s)$ is the curvature of the truncated boundary at the point s , μ_r is the relative permeability of the surrounding medium, and E^{inc} is the incident plane wave. In our simulation, the truncated boundary is a circle with the radius of 6 m. It is 5 m away from the dielectric objects to reduce possible reflection from the truncated boundary, and $\kappa(s)$ is $1/6$.

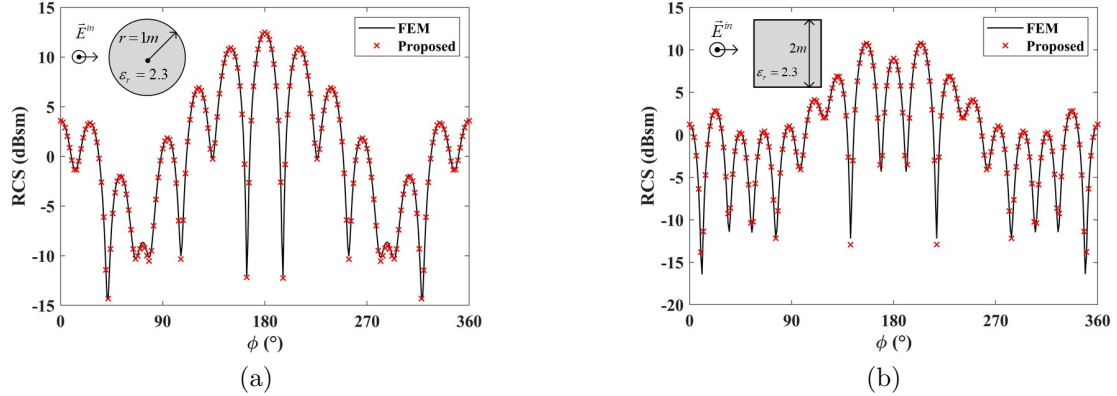


Figure 5: The RCS obtained from the proposed SIE-PDE formulation and the FEM for (a) the dielectric cylinder, and (b) the dielectric cuboid.

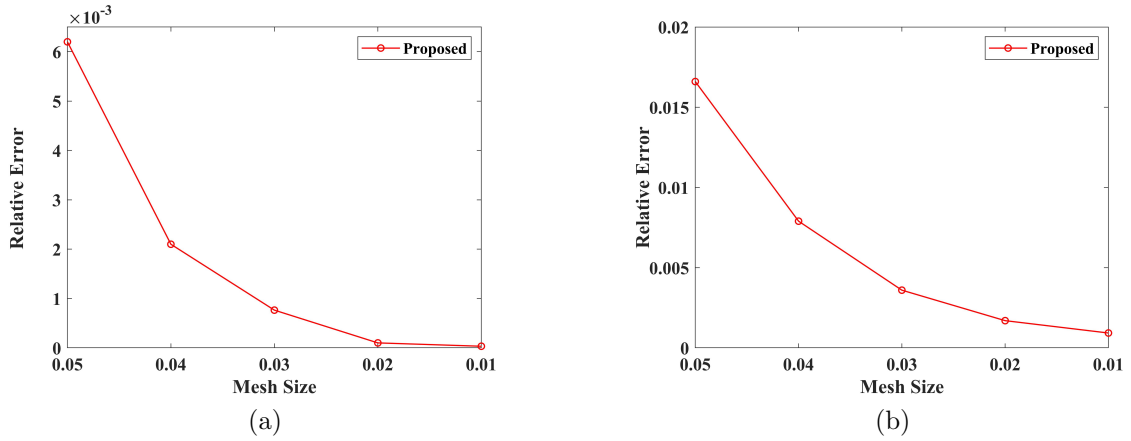


Figure 6: Relative error of the proposed SIE-PDE formulation for (a) the dielectric cylinder, and (b) the dielectric cuboid.

The radius of the cylinder is 1 m and the side length of the cuboid is 2 m. A TM-polarized plane wave incidents from the x -axis with $f = 300$ MHz. The average length of segments used to discretize the whole computational domain is 0.033 m, which corresponds to $\lambda/20$, where λ is the wavelength inside dielectric objects.

Fig. 5 shows the RCS of the two dielectric objects obtained from the proposed hybrid SIE-PDE formulation with the reference RCS obtained from the FEM. It is easy to find that the results obtained from the two formulations for both objects agree well with each other. Therefore, the proposed hybrid SIE-PDE formulation can obtain accurate far fields induced by penetrable objects with smooth and non-smooth boundaries.

Then, we check the convergence property of the proposed SIE-PDE formulation in terms of mesh sizes. The relative error (RE) is defined as

$$\text{RE} = \frac{\sum_i \left\| \text{RCS}^{\text{cal}} - \text{RCS}^{\text{ref}} \right\|^2}{\sum_i \left\| \text{RCS}^{\text{ref}} \right\|^2}, \quad (60)$$

where RCS^{cal} denotes results calculated from the proposed SIE-PDE formulation, and RCS^{ref} is the reference results obtained from the FEM with fine enough meshes. As shown in Fig. 6, it can be found that as the

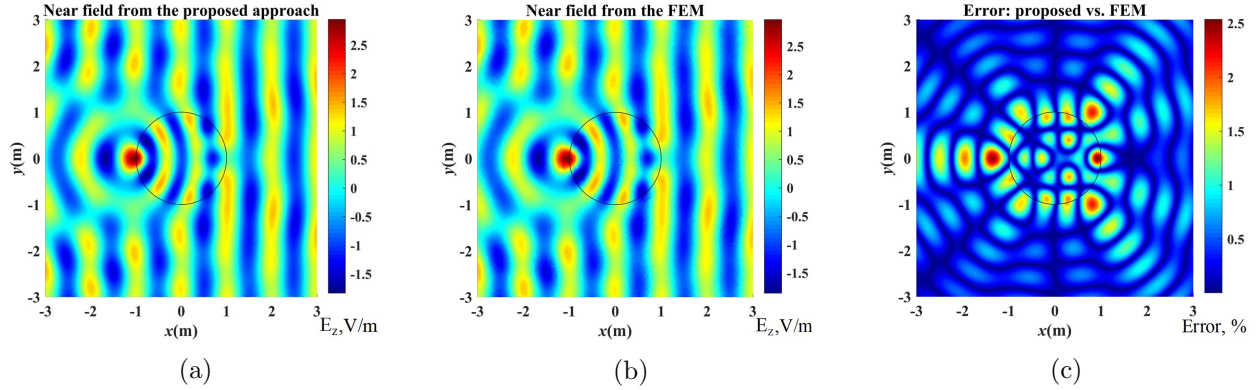


Figure 7: (a) Near fields obtained from the proposed SIE-PDE formulation, (b) near fields obtained from the FEM, and (c) the relative error of near fields obtained from the proposed SIE-PDE formulation and the FEM.

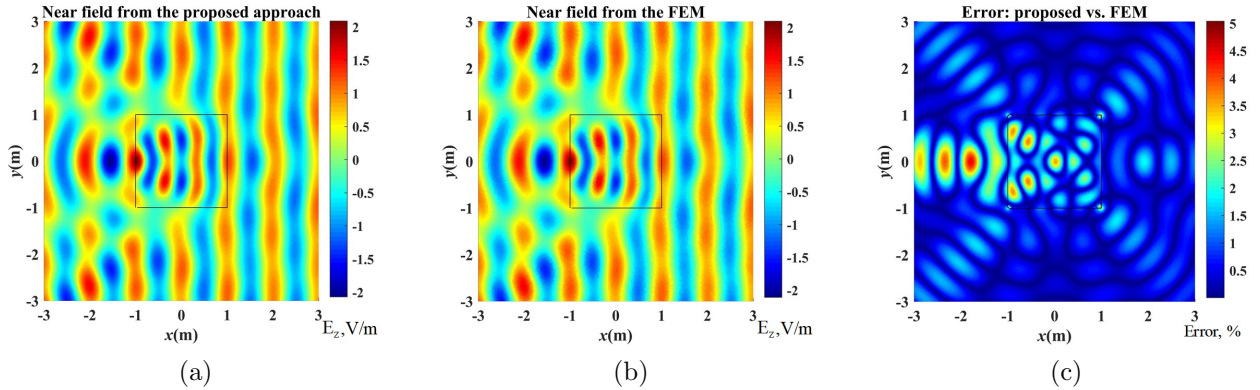


Figure 8: (a) Near fields obtained from the proposed SIE-PDE formulation, (b) near fields obtained from the FEM, and (c) the relative error of near fields obtained from the proposed SIE-PDE formulation and the FEM.

mesh size decreases, the relative error of the proposed SIE-PDE formulation for both objects decreases. For the cylinder object, the RE can reach the order -4 when the average mesh size is 0.01. For the cuboid object, the relative error is 0.001 when the average mesh size is 0.01, which is slightly larger than that of the cylinder object. This is expected since the cuboid object has non-smooth boundary and large fields variations exist near corners of the cuboid. However, they all show excellent agreement for these two formulations. Therefore, the proposed SIE-PDE formulation shows great convergence properties in terms of mesh size.

For further verification, we calculated the electric fields in the near region of both dielectric objects through the proposed SIE-PDE formulation and the FEM in Fig. 7(a) and (b), Fig. 8(a) and (b), respectively. It is easy to find that the field patterns obtained from the two formulations have no visible differences. To quantitatively measure the error between the two formulations, the relative error defined as $\left|E^{\text{cal}} - E^{\text{ref}}\right| / \max \left|E^{\text{ref}}\right|$ is calculated, where E^{ref} , E^{cal} denote the electric fields obtained from the FEM and the proposed SIE-PDE formulation, respectively, and $\max \left|E^{\text{ref}}\right|$ denotes the maximum magnitude of the reference electric field, which guarantees the relative error is well defined in the whole computational domain.

For the dielectric cylinder in Fig. 7(c), the relative error is less than 2% in most of the computational domain and slightly large relative error occurs near the boundary of the dielectric cylinder. It is expected since in those regions fields change sharply due to media discontinuity. For the dielectric cuboid in Fig. 8(c), the relative error in most regions is less than 3% and slightly large near the boundary of the cuboid object, especially at its four corners. However, the maximum of the relative error is still around 4%. Therefore, the

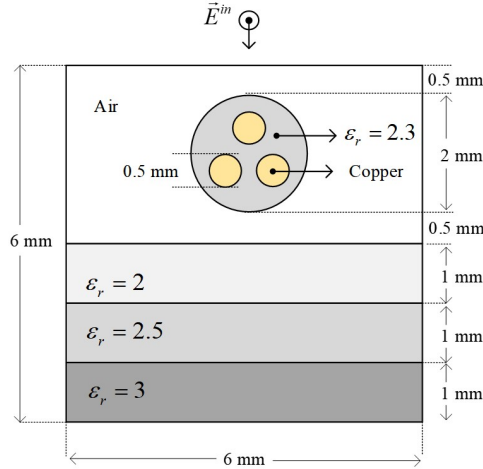


Figure 9: Geometrical configurations of the cable over three planar layered media.

proposed SIE-PDE formulation shows quite good accuracy compared with the FEM.

To sum up, through the numerical results above, we find that the proposed SIE-PDE formulation can accurately calculate both near and far fields induced by dielectric structures with smooth and non-smooth boundaries, and shows great agreement with those obtained from the FEM. To further verify the computational efficiency and accuracy of the proposed SIE-PDE formulation, a more complex structure is considered in next subsection, and the computational costs will be discussed in detail.

5.2. Computational Efficiency and Accuracy Verification of the Proposed Hybrid SIE-PDE Formulation

Due to the skin effect, the current density crowds round the surface region of highly conductive media when the frequency is high. For example, the skin depth of copper at $f = 30$ MHz is approximately $11.9 \mu\text{m}$. In the traditional volumetric mesh formulations, like the FEM, the volume integral equation (VIE) formulation, extremely fine meshes should be used to accurately calculate the current density. For example, to accurately capture the skin effect, almost 40,000 volumetric elements are used for only a $10 \mu\text{m} \times 10 \mu\text{m} \times 10 \mu\text{m}$ copper interconnect at $f = 20$ GHz [43]. Therefore, it is quite challenging to solve this problem in terms of CPU time and memory consumption. Compared with those volumetric meshes based solvers, one obvious merit of the SIE formulations is that they can effectively address computational issues related to conductors and obtain accurate results since unknowns only reside on the boundary of highly conductive media. The proposed hybrid SIE-PDE formulation inherits this merit, and it also increases the flexibility to handle the inhomogeneous media, in which the SIE formulation cannot be used. To further verify the computational efficiency and accuracy of the proposed hybrid SIE-PDE formulation, a numerical example related to conductive media and skin effect calculation is considered. Its geometrical configurations are given in Fig. 9. One cable including three cylindrical copper conductors with the radius of 0.5 mm is placed above the planar layered media. The three cylindrical conductors are embedded in a dielectric sheath with the radius of 1 mm . The relative permittivity of dielectric cylinder is 2.3 . Then, the cable system is placed 0.5 mm over the planar layered media with the relative permittivity of 1 , 2 , 2.5 and 3 , respectively. A TM-polarized plane wave with $f = 30$ MHz incidents along the y -axis.

We calculated electric fields near the object through the proposed SIE-PDE formulation and the FEM, as shown in Fig. 10(a) and (b). It can be found that field patterns from the two formulations are almost the same. To quantitatively measure the error, we also calculated the relative error of near fields. As shown in Fig. 10(c), the relative error is less than 0.5% in most regions of the computational domain and slightly large on the boundary of the inner cylindrical conductors. In the current mesh configuration, both formulations use the same mesh size, 0.05 mm . However, by further calculating the current density in the conductors, the peak values of the current density obtained from the two formulations show significant

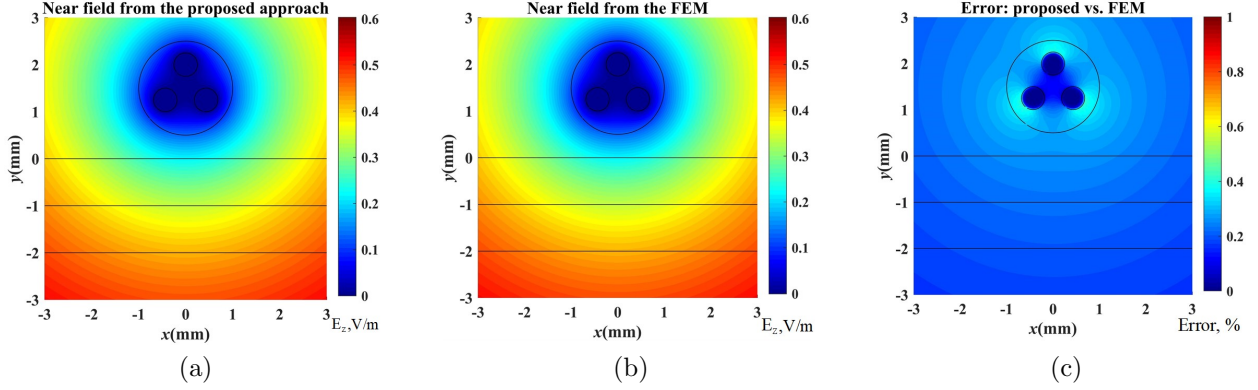


Figure 10: (a) Near fields obtained from the proposed SIE-PDE formulation, (b) near fields obtained from the FEM, and (c) the relative error of near fields obtained from the proposed SIE-PDE formulation and the FEM.

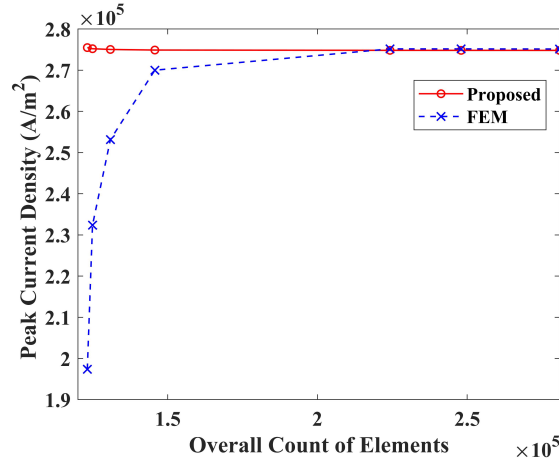


Figure 11: The peak current density obtained from the proposed SIE-PDE formulation and the FEM in terms of the count of elements.

differences. The values obtained from the proposed SIE-PDE formulation and the FEM are $275,492.7 A/m^2$ and $197,378.4 A/m^2$, respectively. Then, we checked the convergence property of the proposed SIE-PDE formulation and the FEM in terms of the current density in Fig. 11. The x -axis represents the overall count of elements in the whole computational domain, and the y -axis represents the peak amplitude of the current density. It can be found that as the count of elements increases, the current density obtained from the FEM gradually increases, and finally is convergent at around $275,000 A/m^2$. However, from the proposed SIE-PDE formulation, the results get the convergent results quite fast with much fewer elements, which implies that the proposed SIE-PDE formulation can obtain the accurate current density with much coarser meshes compared with those of the FEM. When the count of elements reaches approximate 2.3×10^5 , the FEM gets convergent results. For example, when the count of elements is $224,244$, the peak values of the current density obtained from the proposed SIE-PDE formulation and the FEM are $274,827.9 A/m^2$ and $275,180.0 A/m^2$, respectively, and it can be considered that the two formulations reach almost the same level of accuracy.

Fig. 12(a) and (b) show the current density obtained from the proposed SIE-PDE formulation and the FEM. It is easy to find that both formulations can accurately capture the skin effect in terms of the current density, and Table 1 shows the comparison of computational consumption of the two formulations when the current density with the same level of accuracy is obtained. The ratio in the last column of Table 1

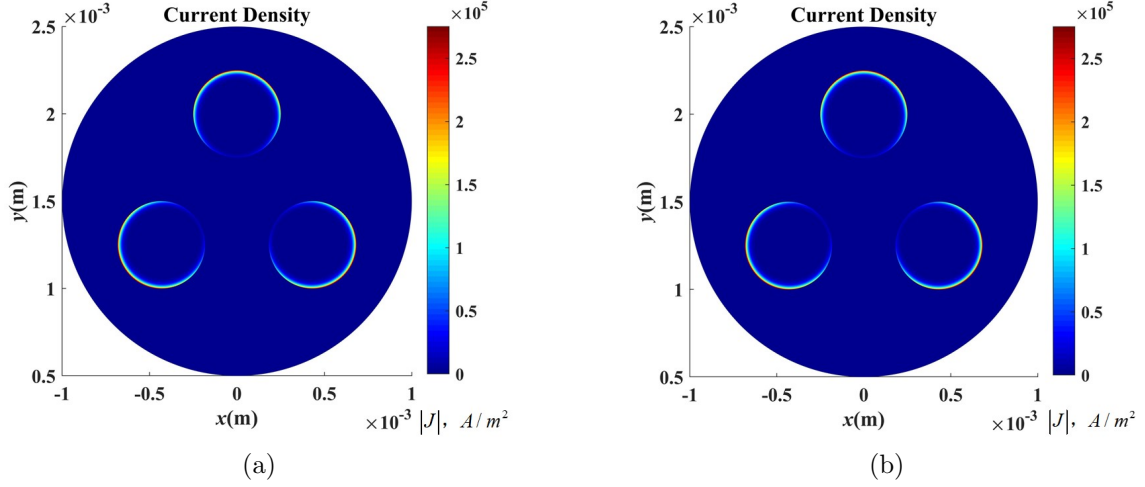


Figure 12: The current density obtained from (a) the proposed SIE-PDE formulation, and (b) the FEM.

Metric	FEM	Proposed	Ratio
Peak Value of Current Density [A/m^2]	274,965.9	274,899.7	0.99
Overall Counts of Unknowns	253,673	73,234	0.29
Memory Consumption [MB]	138.8	50.1	0.36
Total Time [s]	4,771.9	330.4	0.07
Time for \mathbb{Y}_s Generation [s]	-	232.0	-
Time for Matrices Filling [s]	4,769.0	97.7	0.02
Time for Matrices Solving [s]	2.9	0.7	0.24

is defined as the ratio of the values obtained from the proposed SIE-PDE formulation to those from the FEM. As shown in the second row of Table 1, the peak value of the current density is 274,899.7 A/m^2 for the proposed SIE-PDE formulation compared with 274,965.9 A/m^2 for the FEM. Its ratio is 0.9997 and to this extent, the two formulations achieve almost the same level of accuracy. Then, we calculated the overall unknowns used for the two formulations. As shown in the third row of Table 1, the proposed SIE-PDE formulation only needs 73,234 unknowns to solve this problem compared with 253,673 unknowns for the FEM. Its ratio is 0.29, which means that only quite a small fraction of amount of unknowns is required in the proposed SIE-PDE formulation. As is illustrated above, the SIE formulations can capture the skin effect inside the conductors fast and accurately without requirements for fine meshes. In this case, for the FEM the average length of segments is used as 0.005 mm for the inner cylindrical copper conductors and dielectric object and 0.05 mm for outer layered medium. However, in the proposed SIE-PDE formulation, the average length of segments is only 0.02 mm for the inside objects. Therefore, the overall count of unknowns is significantly reduced for the proposed formulation compared with the FEM. Moreover, as shown in the fourth row of Table 1, memory consumption of the proposed SIE-PDE formulation is only 36% of that of the FEM. The time cost for the two formulations is shown from the fifth to eighth rows in Table 1. The time cost includes generation of \mathbb{Y}_s , matrices filling and matrices solving. The time cost for the FEM requires 4,771.9 seconds to solve this problem. However, only 330.4 seconds are required for the proposed formulation, which only requires 7% of CPU time of the FEM. As shown in Table 1, the time cost of matrices filling and solving linear equations is reduced compared with that of the FEM due to much fewer unknowns in the proposed SIE-PDE formulation. As the count of SIE domains increases, the performance improvement in terms of time cost and count of unknowns would be more significant.

6. Conclusion

In this paper, a novel and efficient hybrid SIE-PDE formulation for electromagnetic analysis without boundary condition requirement is developed. In this formulation, the whole computational domain is decomposed into two *overlapping* domains: the SIE and PDE domains. In the SIE domain, complex structures or computationally challenging media are replaced by the background medium, and an equivalent model with only the surface equivalent electric current density on the enclosed boundary is derived to represent electromagnetic effects. Then, the remaining computational domain and the background medium replaced domain consist of the PDE domain and are formulated through the PDE formulation. Through carefully constructing the basis functions, the expansion of the SIE and PDE formulations are compatible on the boundary. Then, a hybrid SIE-PDE formulation is obtained. The proposed formulation shows many advantages over other existing hybrid techniques, such as no extra boundary condition requirements, flexibility and high efficiency in handling complex and computationally challenging structures. Numerical results demonstrate that the proposed SIE-PDE formulation can significantly improve the performance in terms of the count of unknowns and time costs over the FEM, which shows great potential for electromagnetic analysis of complex, non-uniform media fulfilled objects. Currently, development of the proposed SIE-PDE formulation into three-dimensional general scenarios is in progress. We will report more results on this topic.

Acknowledgement

This work was supported in part by the National Natural Science Foundation of China through Grant 61801010, 61671257, 61631002, and Fundamental Research Funds for the Central Universities.

Appendix

In this paper, the Green's function is expressed as $G(\mathbf{r}, \mathbf{r}') = -jH_0^{(2)}(k\rho)/4$, where $j = \sqrt{-1}$, $\rho = |\mathbf{r} - \mathbf{r}'|$, k denotes the wave number in the penetrable object, and $H_0^{(2)}(\cdot)$ denotes the zeroth-order Hankel function of the second kind. When $|k\rho| < 0.1$, the Green's function and its gradient suffer from nearly singular and singular integrals. The first-order small variable approximation of $H_0^{(2)}(\cdot)$ and $H_1^{(2)}(\cdot)$ [44] is considered, which is expressed as

$$H_0^{(2)}(k\rho) \approx \left[1 - j\frac{2}{\pi} \ln\left(\frac{\gamma k}{2}\right) \right] - j\frac{2}{\pi} \ln \rho, \quad (61)$$

$$H_1^{(2)}(k\rho) \approx \frac{k\rho}{2} + \frac{2j}{\pi k\rho}, \quad (62)$$

where $\gamma = 1.781$, $\rho = |\mathbf{r} - \mathbf{r}'|$.

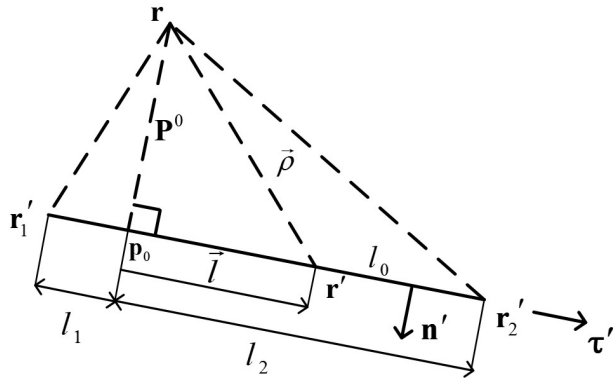


Figure 13: A general configuration to demonstrate the geometrical relationship between the observation point and the source segment. $\vec{\rho} = \mathbf{r} - \mathbf{r}'$, $\tau' = \frac{\mathbf{r}_2' - \mathbf{r}_1'}{|\mathbf{r}_2' - \mathbf{r}_1'|}$, $\vec{l} = \tau' \cdot [(\mathbf{r}' - \mathbf{r}) \cdot \tau']$, $l_0 = |\mathbf{r}_2' - \mathbf{r}_1'|$, $l_1 = (\mathbf{r}_1' - \mathbf{r}) \cdot \tau'$, $l_2 = (\mathbf{r}_2' - \mathbf{r}) \cdot \tau'$, $\mathbf{P}^0 = |\mathbf{p}_0 - \mathbf{r}|$.

A general configuration to demonstrate the geometrical relationship between the observation point and the source segment is shown in Fig. 13. \mathbf{r} , \mathbf{r}' , \mathbf{r}_1' , \mathbf{r}_2' denote the observation point, the source point, and two end points of the source segment, respectively, and \mathbf{p}_0 denotes the projection point of \mathbf{r} on the source segment. As shown in (24), there are two half rooftop basis functions defined on each line segment, $\frac{|\mathbf{r}' - \mathbf{r}_1'|}{l_0}$ and $\frac{|\mathbf{r}_2' - \mathbf{r}'|}{l_0}$, respectively. Therefore, the analytical expression for (32) can be expressed as

$$\begin{aligned} & f_m(\mathbf{r}) \cdot \int_{\mathbf{r}_1'}^{\mathbf{r}_2'} j\omega\mu G_1(\mathbf{r}, \mathbf{r}') \cdot \frac{|\mathbf{r}' - \mathbf{r}_1'|}{l_0} d\mathbf{r}' \\ &= f_m(\mathbf{r}) \cdot \left\{ \frac{\omega\mu}{4l_0} \left[1 - j\frac{2}{\pi} \ln\left(\frac{\gamma k}{2}\right) \right] \cdot I_1 - j\frac{\omega\mu}{2\pi l_0} \cdot I_2 + j\frac{\omega\mu}{2\pi l_0} l_1 \cdot I_3 - \frac{\omega\mu l_1}{4l_0} \left[1 - j\frac{2}{\pi} \ln\left(\frac{\gamma k}{2}\right) \right] \cdot I_4 \right\}, \end{aligned} \quad (63)$$

$$\begin{aligned} & f_m(\mathbf{r}) \cdot \int_{\mathbf{r}_1'}^{\mathbf{r}_2'} j\omega\mu G_1(\mathbf{r}, \mathbf{r}') \cdot \frac{|\mathbf{r}_2' - \mathbf{r}'|}{l_0} d\mathbf{r}' \\ &= f_m(\mathbf{r}) \cdot \left\{ -\frac{\omega\mu}{4l_0} \left[1 - j\frac{2}{\pi} \ln\left(\frac{\gamma k}{2}\right) \right] \cdot I_1 + j\frac{\omega\mu}{2\pi l_0} \cdot I_2 - j\frac{\omega\mu}{2\pi l_0} l_2 \cdot I_3 + \frac{\omega\mu l_2}{4l_0} \left[1 - j\frac{2}{\pi} \ln\left(\frac{\gamma k}{2}\right) \right] \cdot I_4 \right\}, \end{aligned} \quad (64)$$

and the analytical expression for (33) can also be obtained as

$$\begin{aligned} & f_m(\mathbf{r}) \cdot \int_{\mathbf{r}_1'}^{\mathbf{r}_2'} k \frac{\vec{\rho} \cdot \mathbf{n}'}{\rho} G_1'(\mathbf{r}, \mathbf{r}') \frac{|\mathbf{r}' - \mathbf{r}_1'|}{l_0} d\mathbf{r}' \\ &= f_m(\mathbf{r}) \cdot \left\{ \frac{jk^2}{8l_0} \mathbf{P}^0 \cdot I_1 - \frac{jk^2}{8l_0} \mathbf{P}^0 l_1 \cdot I_4 - \frac{\mathbf{P}^0}{2\pi l_0} \cdot I_5 + \frac{\mathbf{P}^0}{2\pi l_0} l_1 \cdot I_6 \right\}, \end{aligned} \quad (65)$$

$$\begin{aligned} & f_m(\mathbf{r}) \cdot \int_{\mathbf{r}_1'}^{\mathbf{r}_2'} k \frac{\vec{\rho} \cdot \mathbf{n}'}{\rho} G_1'(\mathbf{r}, \mathbf{r}') \frac{|\mathbf{r}_2' - \mathbf{r}'|}{l_0} d\mathbf{r}' \\ &= f_m(\mathbf{r}) \cdot \left\{ -\frac{jk^2}{8l_0} \mathbf{P}^0 \cdot I_1 + \frac{jk^2}{8l_0} \mathbf{P}^0 l_2 \cdot I_4 + \frac{\mathbf{P}^0}{2\pi l_0} \cdot I_5 - \frac{\mathbf{P}^0}{2\pi l_0} l_2 \cdot I_6 \right\}. \end{aligned} \quad (66)$$

According to [44][45], the six identities defined in (63)-(66) are given as below.

$$I_1 = \int_{l_i} |\vec{l}| d\mathbf{r}' = \frac{1}{2} \left[(l_2)^2 - (l_1)^2 \right], \quad (67)$$

$$I_2 = \int_{l_i} \vec{l} \cdot \ln|\mathbf{r} - \mathbf{r}'| d\mathbf{r}' = \frac{\vec{\tau}}{2} \left\{ |\mathbf{r} - \mathbf{r}_2'|^2 \ln|\mathbf{r} - \mathbf{r}_2'| - |\mathbf{r} - \mathbf{r}_1'|^2 \ln|\mathbf{r} - \mathbf{r}_1'| - \frac{1}{2} \left[(l_2)^2 - (l_1)^2 \right] \right\}, \quad (68)$$

$$I_3 = \int_{l_i} \ln|\mathbf{r} - \mathbf{r}'| d\mathbf{r}' = l_2 \ln|\mathbf{r} - \mathbf{r}_2'| - l_1 \ln|\mathbf{r} - \mathbf{r}_1'| + \mathbf{P}^0 \left(\tan^{-1} \frac{l_2}{\mathbf{P}^0} - \tan^{-1} \frac{l_1}{\mathbf{P}^0} \right) - (l_2 - l_1), \quad (69)$$

$$I_4 = \int_{l_i} 1 d\mathbf{r}' = l_2 - l_1, \quad (70)$$

$$I_5 = \int_{l_i} \frac{|\vec{l}|}{|\mathbf{r} - \mathbf{r}'|^2} d\mathbf{r}' = \frac{1}{2} \left(\ln|\mathbf{r} - \mathbf{r}_2'|^2 - \ln|\mathbf{r} - \mathbf{r}_1'|^2 \right), \quad (71)$$

$$I_6 = \int_{l_i} \frac{1}{|\mathbf{r} - \mathbf{r}'|^2} d\mathbf{r}' = \frac{1}{\mathbf{P}^0} \cdot \left[\tan^{-1} \left(\frac{l_2}{\mathbf{P}^0} \right) - \tan^{-1} \left(\frac{l_1}{\mathbf{P}^0} \right) \right]. \quad (72)$$

References

- [1] Z. Peng, K. Lim, J. Lee, Nonconformal Domain Decomposition Methods for Solving Large Multiscale Electromagnetic Scattering Problems, *Proc. IEEE* 101 (2) (Feb. 2013), 298-319, <https://doi.org/10.1109/JPROC.2012.2217931>.
- [2] S. D. Gedney, J. Lee and R. Mittra, A combined FEM/MoM approach to analyze the plane wave diffraction by arbitrary gratings, *IEEE Trans. Microw. Theory Tech.* 40 (2) (Feb. 1992): 363-370, <https://doi.org/10.1109/22.120110>
- [3] F. L.Teixeira, FDTD/FETD methods: a review on some recent advances and selected applications, *J. Microwaves Optoelectr.*, 6 (1) (Aug. 2007), pp. 83-95.
- [4] M. S. Yeung, Application of the hybrid FDTD-FETD method to dispersive materials, *Microw. Opt. Tech. Lett.* 23 (4) (Oct. 1999) 238-242, [https://doi.org/10.1002/\(SICI\)1098-2760\(19991120\)23:4<238::AID-MOP15;3.0.CO;2-0](https://doi.org/10.1002/(SICI)1098-2760(19991120)23:4<238::AID-MOP15;3.0.CO;2-0)
- [5] Q. Sun, R. Zhang, Q. Zhan, Q. Liu, 3-D Implicit-Explicit Hybrid Finite Difference/Spectral Element/Finite Element Time Domain Method Without a Buffer Zone, *IEEE Trans. Antennas Propag.* 67 (8) (Aug. 2019) 5469-5476, <https://doi.org/10.1109/TAP.2019.2913740>.
- [6] K. Fan, B. Wei, X. He, The implement of the hybrid meshes in US-FETD by using Domain decomposition method, in: *Numerical Electromagnetic and Multiphysics Modeling and Optimization for RF, Microwave, and Terahertz Application (NEMO)*, 2020 IEEE MTT-S International Conference on, IEEE, pp. 1-3.
- [7] K. Zhang, C. Wang, J. Jin, A hybrid FETD-GSM algorithm for broadband full-wave modeling of resonant waveguide devices, *IEEE Trans. Microw. Theory Tech.* 65 (9) (Sept. 2017) 3147-3158, <https://doi.org/10.1109/TMTT.2017.2687423>.
- [8] A. Aydođan, A hybrid MoM/MM method for fast analysis of E-plane dielectric loaded waveguides, *AEU-Int. J. Electron. C.* 100 (2019) 9-15.
- [9] E. Diaz Caballero, H. Esteban, A. Belenguer, V. E. Boria, J. V. Morro, J. Cascon, Efficient design of substrate integrated waveguide filters using a hybrid MoM/MM analysis method and efficient rectangular waveguide design tools, in: *Electromagnetics in Advanced Applications(ICEAA)*, 2011 International Conference on, IEEE, 2011, pp. 456-459.
- [10] M. Chen, Y. Zhang, X. Zhao, C. Liang, Analysis of antenna around NURBS surface with hybrid MoM-PO technique, *IEEE Trans. Antennas Propag.* 55 (2) (Feb. 2007) 407-413, <https://doi.org/10.1109/TAP.2006.889814>
- [11] L. Xiao, X. Wang, B. Wang, G. Zheng, P. Chen, An efficient hybrid method of iterative MoM-PO and equivalent dipole-moment for scattering from electrically large objects, *IEEE Antennas Wireless Propag. Lett.* 16 (Feb. 2017) 1723-1726, <https://doi.org/10.1109/LAWP.2017.2669910>.
- [12] Z. Gong, B. Xiao, G. Zhu, H. Ke, Improvements to the hybrid MoM-PO technique for scattering of plane wave by an infinite wedge, *IEEE Trans. Antennas Propag.* 54 (1) (Jan. 2006) 251-255, <https://doi.org/10.1109/TAP.2005.861511>.
- [13] M. M. Ilic, M. Djordjevic, A. Z. Ilic, B. M. Notaro, Higher order hybrid FEM-MoM technique for analysis of antennas and scatterers, *IEEE Trans. Antennas Propag.* 57 (5) (May 2009) 1452-1460, <https://doi.org/10.1109/TAP.2009.2016725>.
- [14] D. J. Hoppe, L. W. Epp, J. Lee, A hybrid symmetric FEM/MOM formulation applied to scattering by inhomogeneous bodies of revolution, *IEEE Trans. Antennas Propag.* 42 (6) (Jun. 1994) 798-805, <https://doi.org/10.1109/8.301698>.
- [15] R. Xu, L. Guo, H. He, W. Liu, A hybrid FEM/MoM technique for 3-D electromagnetic scattering from a dielectric object above a conductive rough surface, *IEEE Geosci. Remote Sens. Lett.* 13 (3) (Mar. 2016) 314-318, <https://doi.org/10.1109/LGRS.2015.2508500>.
- [16] Y. Ren, Q. Liu and Y. Chen, A hybrid FEM/MoM method for 3-D electromagnetic scattering in layered medium, *IEEE Trans. Antennas Propag.* 64 (8) (Aug. 2016) 3487-3495, <https://doi.org/10.1109/TAP.2016.2575979>.
- [17] M. M. Ilic, B. M. Notaros, Higher order FEM-MoM domain decomposition for 3-D electromagnetic analysis, *IEEE Antennas Wireless Propag. Lett.* 8 (Aug. 2009) 970-973, <https://doi.org/10.1109/LAWP.2009.2030139>.
- [18] Y. Ji, T. H. Hubing, On the modeling of a gapped power-bus structure using a hybrid FEM/MoM approach, " *IEEE Trans. Electromagn. Compat.* 44 (4) (Nov. 2002) 566-569, <https://doi.org/10.1109/TEMC.2002.804775>.
- [19] K. Tap, T. Lertwiriyaprapa, P. H. Pathak, K. Sertel, A hybrid MoM-UTD analysis of the coupling between large multiple arrays on a large platform, in: *2005 IEEE Antennas and Propagation Society International Symposium*, vol. 4, Jul. 2005, pp. 175-178.
- [20] Z. Liu, J. Yang, C. Liang, The hybrid higher order MoM-UTD formulation for electromagnetic radiation problems, *Microwave Opt. Technol. Lett.* 52 (5) (Mar. 2010) 1087-1091, <https://doi.org/10.1002/mop.25125>.
- [21] T. F. Eibert, J. L. Volakis, D. R. Wilton, D. R. Jackson, Hybrid FE/BI modeling of 3-D doubly periodic structures utilizing triangular prismatic elements and an MPIE formulation accelerated by the Ewald transformation, *IEEE Trans. Antennas Propag.* 47 (5) (May 1999) 843-850, <https://doi.org/10.1109/8.774139>.
- [22] X. Q. Sheng, E. K. Yung, Implementation and experiments of a hybrid algorithm of the MLFMA-enhanced FE-BI method for open-region inhomogeneous electromagnetic problems, *IEEE Trans. Antennas Propag.* 50 (2) (Feb. 2002) 163-167, <https://doi.org/10.1109/8.997987>.
- [23] F. J. C. Meyer, The Two-Dimensional finite element/boundary element method in electromagnetics: formulation applications error estimates and mesh adaptive procedures, Ph.D. dissertation, Univ. Stellenbosch, South Africa, 1994.
- [24] K. Zhao, M. N. Vouvakis, J. Lee, Solving electromagnetic problems using a novel symmetric FEM-BEM approach, h," *IEEE Trans. Magn.* 42 (4) (Apr. 2006) 583-586, <https://doi.org/10.1109/TMAG.2006.872489>.
- [25] M. Yang, H. Gao, X. Sheng, Parallel domain-decomposition-based algorithm of hybrid FE-BI-MLFMA method for 3-D scattering by large inhomogeneous objects, *IEEE Trans. Antennas Propag.* 61 (9) (Sep. 2013) 4675-4684, <https://doi.org/10.1109/TAP.2013.2271232>.
- [26] M. N. Vouvakis, S. Lee, K. Zhao, J. Lee, A symmetric FEM-IE formulation with a single-level IE-QR algorithm for solving electromagnetic radiation and scattering problems, *IEEE Trans. Antennas Propag.* 52 (11) (Nov. 2004): 3060-3070, <https://doi.org/10.1109/TAP.2004.837525>.
- [27] J. Guan, S. Yan, J. Jin, A multi-solver scheme based on combined field integral equations for electro-

- magnetic modeling of highly complex objects, *IEEE Trans. Antennas Propag.* 65 (3) (Mar. 2017) 1236-1247, <https://doi.org/10.1109/TAP.2017.2657492>.
- [28] J. Guan, S. Yan, J. Jin, A multisolver scheme based on robin transmission conditions for electromagnetic modeling of highly complex objects, *IEEE Trans. Antennas Propag.* 64 (12) (Dec. 2016) 5345-5358, <https://doi.org/10.1109/TAP.2016.2618543>.
- [29] J. Jin, *The Finite Element Method in Electromagnetics*. Hoboken, NJ, USA: Wiley, 2014.
- [30] S. Lee, M. N. Vouvakis, J. Lee, A non-overlapping domain decomposition method with non-matching grids for modeling large finite antenna arrays, *J. Comput. Phys.* 203 (1) (Feb. 2005) 1-21, <https://doi.org/10.1016/j.jcp.2004.08.004>.
- [31] B. Stupfel, Martine Mognot, A domain decomposition method for the vector wave equation, *IEEE Trans. Antennas Propag.* 48 (5) (May 2000) 653-660, <https://doi.org/10.1109/8.855483>.
- [32] Z. Peng, X. Wang, J. Lee, Integral equation based domain decomposition method for solving electromagnetic wave scattering from non-penetrable objects, *IEEE Trans. Antennas Propag.* 59 (9) (Sep. 2011) 3328-3338, <https://doi.org/10.1109/TAP.2011.2161542>.
- [33] K. Zhao, V. Rawat, J. Lee, A domain decomposition method for electromagnetic radiation and scattering analysis of multi-target problems, *IEEE Trans. Antennas Propag.* 56 (8) (Aug. 2008) 2211-2221, <https://doi.org/10.1109/TAP.2008.926774>.
- [34] J. Lu, Y. Chen, D. Li, J. Lee, An embedded domain decomposition method for electromagnetic modeling and design, *IEEE Trans. Antennas Propag.* 67 (1) (Jan. 2018) 309-323, <https://doi.org/10.1109/TAP.2018.2874751>.
- [35] J. Lu, J. Lee, Signal integrity analysis of integrated circuits by using embedded domain decomposition method, *IEEE Trans. Microw. Theory Tech.* 66 (12) (Dec. 2018) 5369-5382, <https://doi.org/10.1109/TMTT.2018.2874639>.
- [36] C. Balanis, *Antenna Theory: Analysis and Design*, 3rd ed. Wiley, 2005.
- [37] X. Zhou, Z. Zhu, S. Yang, Towards a unified approach to electromagnetic analysis of objects embedded in multilayers, *J. Comput. Phys.* 427 (Feb. 2021) 110073, <https://doi.org/10.1016/j.jcp.2020.110073>.
- [38] T. Okoshi, *Planar Circuits for Microwaves and Lightwaves*, Springer Berlin Heidelberg, 1985.
- [39] U. R. Patel, P. Triverio, S. V. Hum, A single-source surface integral equation formulation for composite dielectric objects, in: 2017 IEEE Antennas and Propagation Society International Symposium, Jul. 2017, pp. 1453-1454.
- [40] L. Knockaert, D. De Zutter, G. Lippens, H. Rogier, On the Schur complement form of the Dirichlet-to-Neumann operator, *Wave Motion* 45 (3) (Jan. 2008) 309-324, <https://doi.org/10.1016/j.wavemoti.2007.07.004>.
- [41] U. R. Patel, P. Triverio, Skin effect modeling in conductors of arbitrary shape through a surface admittance operator and the contour integral method, *IEEE Trans. Microw. Theory Tech.* 64 (9) (Aug. 2016) 2708-2717, <https://doi.org/10.1109/TMTT.2016.2593721>.
- [42] X. Zhou, Z. Zhu, S. Yang, Formulation of Single-Source Surface Integral Equation for Electromagnetic Analysis of 2D Partially Connected Penetrable Objects, *IEEE J. Multiscale and Multiphys. Comput. Techn.* 6 (Jan. 2021) 16-23, <https://doi.org/10.1109/JMMCT.2021.3052890>.
- [43] M. A. I. AlQedra, Surface impedance formulation for electric field integral equation in magneto-quasistatic and full-wave boundary element models of interconnects, 2010.
- [44] D. Wilton, S. Rao, A. Glisson, D. Schaubert, O. Al-Bundak, C. Butler, Potential integrals for uniform and linear source distribution on polygonal and polyhedral domains, *IEEE Trans. Antennas Propag.* 32 (3) (Mar. 1984) 276-281, <https://doi.org/10.1109/TAP.1984.1143304>.
- [45] J. Stewart, *Calculus*, Brooks Cole, 2007.